Journal of the Meteorological Society of Japan, Vol. 91, No. 5, pp. 609–626, 2013
DOI:10.2151/jmsj.2013-504

Behavior and Structure of Convective Clouds Developing around a Mountainous Area Observed by Stereo Photogrammetry and Ka-Band and X-Band Radars: Case Study of Northern Kanto, Japan

Natsuki NISHIWAKI

Graduate School of Life and Environmental Sciences, University of Tsukuba, Tsukuba, Japan

Ryohei MISUMI, Shingo SHIMIZU, Takeshi MAESAKA, Koyuru IWANAMI, Namiko SAKURAI, Masayuki MAKI, Shin-ichi SUZUKI, Atsushi KATO

National Research Institute for Earth Science and Disaster Prevention, Tsukuba, Japan

and

Akihiko YAMAJI

Japan Weather Association, Tokyo, Japan

(Manuscript received 5 December 2011, in final form 18 May 2013)

Abstract

Development of convective clouds on August 24, 2009 in northern Kanto, Japan, was investigated using stereo photogrammetric analysis and Ka-band and X-band radars, in order to clarify the behavior and structure of convective clouds developing around a mountainous area. Convective activity was divided into three stages based on the spatial distribution of X-band radar echoes: stage 1 with no echo (1006-1200 JST), stage 2 with echoes limited to the mountainous area (1200-1400 JST), and stage 3 with echoes developing over the plain (1400-1600 JST). During stages 1 and 2, the convective clouds (echoes) initiated over the mountains, and then moved toward the foot of mountains and dissipated, repeatedly. During stage 3, convective echoes formed over the mountains moved to the plain without dissipating at the foot of the mountains. In stage 2, new convective echoes tended to form to the rear (upshear) side of pre-existing echoes, while in stage 3, some new cellular echoes formed to the front (downshear) side of pre-existing echoes. Specific humidity in the mountains increased in stage 1, while GPS-derived precipitable water at the foot of the mountains increased during stages 2 and 3. The relationship between the behavior of convective clouds and the transport of water vapor by local wind circulation is discussed.

Keywords convective cloud; thermally induced circulation; sea breeze

1. Introduction

Convective clouds developing over mountainous areas in summer cause heavy local-scale rainfall and often lead to floods. Previous studies have shown that convective clouds frequently form in mountainous areas in the early afternoon and then move toward plain areas (e.g., Saito and Kimura 1998; Horie and Tomine 1998; Kojima and Iwasaki 2001; Sawada and Takahashi 2002). The small scale of convective clouds relative to synoptic-scale disturbances makes it

Corresponding author: Natsuki Nishiwaki, Graduate School of Life and Environmental Sciences, University of Tsukuba, 1-1 Tennodai, Tsukuba 305-8577, Japan
E-mail: nishiwaki@geoenv.tsukuba.ac.jp

difficult to simulate or forecast convective cloud development using a cloud-resolving model (e.g., Nakamura et al. 2011). To improve numerical forecasting of convective clouds, understanding the behavior and structure of convective clouds around mountainous areas is important. This study provides a detailed description of the behavior and structure of convective clouds developing around mountains using various instruments.

The environmental conditions under which summertime convective clouds develop have been previously analyzed by several studies. Fujibe et al. (2003) used the fuzzy c-means method to classify the rainfall distribution over the Kanto plain, Japan. They showed that when rainfall occurred over northern Kanto, the Kanto plain was dominated by the southerly sea breeze and the convergence in the center of the plain was slightly larger than that on days without rainfall. Kimura and Kuwagata (1995) pointed out that the difference of sensible heating between the air over valleys and mountains leads to valley wind circulation, which transports water vapor from valleys to mountains. Kondo (1990a, b) asserted that the valley wind and the sea breeze unite to form an "extended" sea breeze around the Kanto plain, which connects the airflow from the shore to the inland. Iwasaki (2004) showed that GPS precipitable water had dual maxima around Mt. Tanigawa on sunny summer days in the daytime and evening and that the dual maxima correspond to convective activity peaks. The daytime maximum was due to water vapor transported by valley wind circulation, and the evening maximum corresponded to water vapor convergence of the extended sea breeze. In addition, analysis using a numerical model and GPS precipitable water showed that the high precipitable water around the mountainous area tended to move toward the plain (Sato and Kimura 2003, 2005). According to these studies, the movement of the high GPS precipitable water region and the spatial distribution of radar echoes agree well; thus, this phenomenon can be explained by water vapor advection from the mountains to the plain due to the environmental wind. Hence, these previous studies had clarified the variation of environmental conditions causing the development of convective clouds; however, detailed behavior and structure of individual convective clouds are still not clear.

In contrast to many previous studies focusing on environmental conditions of summertime convection, observational studies of convective cloud behavior are limited because such studies demand organized and intensive field observation using several Doppler radars, cloud radars, and soundings. Sano and Tsuboki (2006) conducted detailed observation of developed convective clouds using dual X-band Doppler radars around the Nobi Plain and Ibuki Mountains, Japan. They discussed the role of the interaction between valley wind circulation and sea breeze for the development and change of structure of cumulonimbus, and concluded that the arrival of sea breeze at the mountain slope under the valley wind circulation triggered the intensive development of the cumulonimbus. In Europe, the Convective and Orographically induced Precipitation Study (COPS) was conducted from July to August 2007 around the Black Forest, which is a broad region around southern Germany and eastern France including mountainous areas. One of the results of this study suggests that the interaction of the thermally induced local circulation and the mesoscale convergence zone is an important trigger for the formation of strong updraft that can intrude into the stable layer with a small convective available potential energy (CAPE) condition (Kalthoff et al. 2009; Barthlott et al. 2010; Bennett et al. 2011). In the United States, the Cumulus, Photogrammetric, In situ, and Doppler Observation Experiment (CUPIDO) investigated convection from a very early stage using stereo photogrammetric analysis, soundings, and airborne sensor observation around the Santa Catalina Mountains, Arizona (Zhender et al. 2007). They concluded that successive formation of convective clouds created appropriate conditions for deep convection (Zhender et al. 2009). The above studies suggest that convective clouds around mountains are strongly affected by valley wind circulation, sea breeze, mesoscale convergence, and modification of atmospheric conditions by clouds. We need to accumulate case studies in various conditions to understand the behavior and structure of convective clouds developing over mountains.

Northern Kanto is a good field to study cumulonimbi because the extended sea breeze often triggers deep convection over the mountains. In this study, we conducted an observation of convective clouds around the mountainous area in northern Kanto using two X-band Doppler radars, a Ka-band radar, and stereo photogrammetric analysis. This study is a challenging observation utilizing various methods to describe convective systems from the early stage to the mature stage. Japan Standard Time (JST = UTC + 09) is used in this paper.

2. Observation

2.1 Instruments and data

The arrangement of observational instruments and ranges during this study are shown in Fig. 1. Two digital cameras are installed to calculate the locations and height of convective clouds using stereo photogrammetric analysis. The cameras (RICOH CX-1) take images at 2592 × 1944 (5 million pixels) resolution at 1-min intervals. The cameras were installed at Care House Namegawa (36.5958°N, 139.7386°E) and on the roof top of the Kanuma Civic Culture Center (36.5708°N, 139.7380°E) at a distance of 2.8 km from Care House.

Stereo photogrammetric analysis is a method to calculate the position (distance and height from each camera) of targets using two images taken from separate places. In this analysis, the common points of the asperity of clouds were identified in each photographic image. Then, the positions of the common points were calculated by triangular surveying using azimuth and elevation angles from the two cameras determined by the coordinate of pixels (x, y) of the images. The relationship between coordinate of the pixels and azimuth and elevation angles was calibrated by measurement using a theodolite before the analysis. Due to the errors caused by lens distortion and readout of common points, there were some differences between the cloud heights calculated from each of the two cameras. If the ratio between the absolute values of the difference and the mean cloud height was larger than 20%, we judged that the data has error and omitted it from the analysis.

The Ka-band radar (transmission frequency: 35 GHz, beam width: 0.28°) owned by the National Research Institute for Earth Science and Disaster Prevention (NIED) was installed at Care House Naegawa in Kanuma City (36.5958°N, 139.7386°E). Because this radar has higher sensitivity and spatial resolution than X-band radars, it was expected to detect cloud droplets that cannot be observed by X-band radars. The observational range (radius) of this radar is 30 km. The Ka-band radar was generally operated in sector scan mode at elevation angles of 5, 8, and 12 degrees at arbitrary time intervals; in cases of occurrence of significant echoes, range height indicator (RHI) observation was performed manually. Unfortunately, the radar sensitivity was decreased by about 12 dBZ due to some problem in the observation, though high spatial resolution data were obtained. In this study, we analyzed the RHI observation data to elucidate the detailed structure of convective echoes.

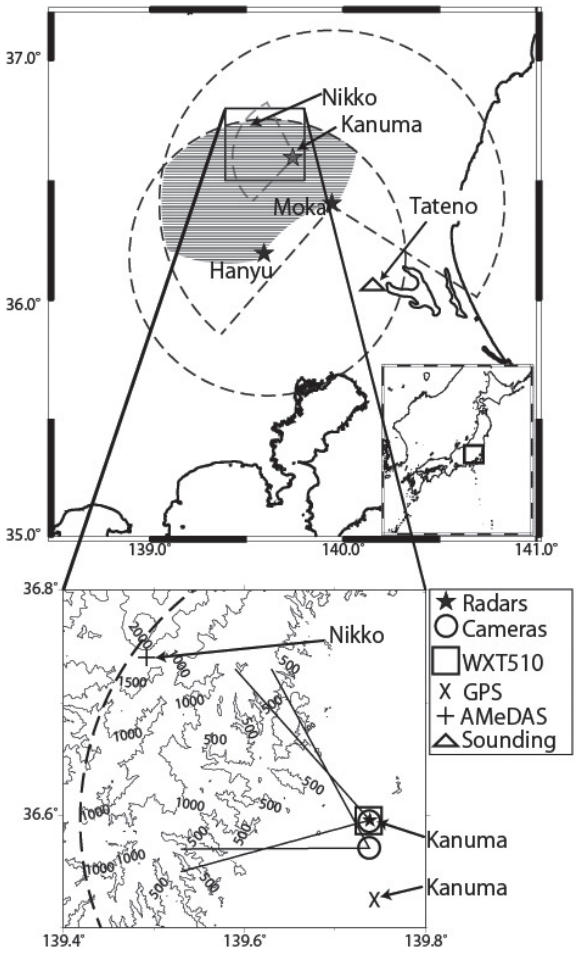

Fig. 1. Arrangement of observation instruments in Kanto, Japan. The sectors and the circles with dashed lines indicate the observation areas of the Ka-band radar (Kanuma) and X-band radars (Moka and Hanyu). The shaded area is the theoretical range of dual Doppler analysis. Bold lines in the lower figure indicate the observation angles of stereo cameras. Topographic contours are drawn at 500-m intervals.

The observation data is distributed in polar coordinates expressed by distance and elevation angle from the radar, and thus we performed nearest neighbor interpolation onto a 0.2 × 0.2 km grid. This spatial resolution is finer than that of the X-band radars, allowing examination of the detailed structure of convective echoes. Due to the problem mentioned above, all of the observed reflectivity was increased by 12 dBZ.

In this study, radar reflectivity and wind vectors deduced by dual X-band Doppler radars were used.

The polarimetric X-band radar owned by NIED was installed at Moka (36.4049°N, 139.9408°E). This radar performed plan position indicator (PPI) volume scans at 5-min intervals. The scan stepped up from 0.7 to 16.4 degrees with 17 elevation angles. The other X-band radar owned by Japan Weather Association (JWA) was installed at Hanyu (36.1952°N, 139.5894°E). This radar also performed PPI volume scans at 5-min intervals. The scan of this radar stepped up from 0.7 to 12.9 degrees with 9 elevation angles. For analysis of the X-band radar data, we converted the reflectivity and Doppler velocity obtained from each radar into 1 × 1 × 0.25 km of Constant Altitude PPI (CAPPI) by Cressman interpolation (Cressman 1959). For reflectivity, only the X-band radar located at Moka was used because attenuation correction was conducted using polarimetric parameters by the method of Park et al. (2005). For calculation of wind vectors, the three-dimensional variational method used by Shimizu and Maesaka (2007) was applied. This is a modification of the method of Gao and Xue (1999). For reduction of calculation cost, the variational method was applied after creating CAPPI data. We assumed the vertical velocity to be zero at the top and bottom of the Doppler velocity observation layer. The time representing each CAPPI is the center time of volume scan: for instance, if the volume scan is conducted from 1200-1205 JST, then the time is represented as 1202 JST.

A weather transmitter WXT510 made by Vaisala was installed at the Ka-band radar site (Kanuma) for surface measurement. Temperature, relative humidity, and air pressure were measured at 1-min intervals by this instrument. In addition, we calculated the precipitable water at Kanuma City using GPS atmosphere delay data of GEO-NET operated by GSI by the method of Naito (1998). Although GPS observation occurred at 10-min intervals, we obtained surface temperature and atmospheric pressure for the calculation of dry atmospheric delay from the initial values of the JMA Mesoscale Model (MSM) every three hours. Thus, precipitable water was calculated at 3-hour intervals. Meteorological surface data observed by Automated Meteorological Data Acquisition System (AMeDAS), upper sounding data at Tateno (36.057°N, 140.125°E), weather charts, and Radar/Raingauge Analyzed Precipitation data provided by JMA were also used for the analysis.

2.2 *Analysis period*

Intensive observation for this study had been conducted from August 8 to 28, 2009. According to AMeDAS data, the climate of August 2009 was characterized by low temperatures and was cloudy. For example, at Utsunomiya Local Meteorological Observatory (located about 15 km northwest of the X-band radar site of Moka), the anomalies (and the absolute value) of monthly mean temperature, total rainfall amount, and sunshine duration were −0.5°C (24.9°C), −32 mm (137 mm), and −23% (114.8 h), respectively. The only day that strong convective activity was observed in the daytime and successfully captured by the cameras was August 24, which was thus chosen as the case of our study. The analysis period was 1006-1600 JST, which includes the period from the beginning of the observation to the time when the radar echoes had left the observation range.

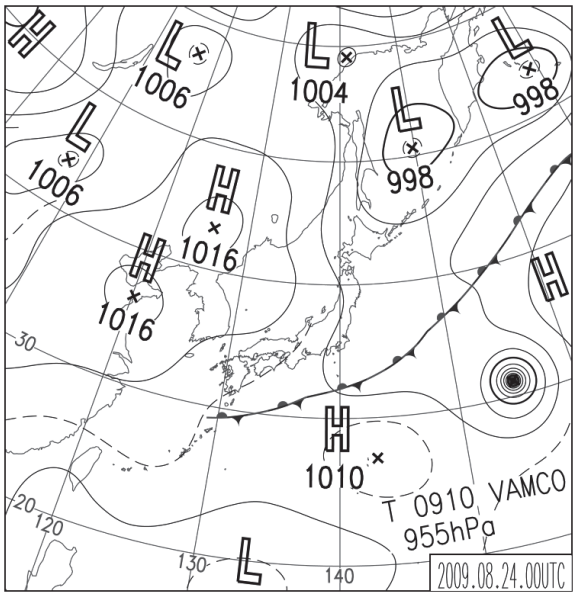

Fig. 2. Surface weather chart at 0900 JST on August 24, 2009 (after Japan Meteorological Agency monthly report).

3. Results

3.1 *Synoptic condition and soundings*

Figure 2 shows the surface weather chart at 0900 JST on August 24. From this figure, a stationary front elongated from an extratropical low was situated in the ocean to the east of Japan, and a migratory high was approaching from the west. The Kanto area is located behind the extratropical low. According to the 500-hPa weather chart at the time, Japan was situated under a cold trough and the northern Kanto area was covered with −9°C air at the 500-hPa level (figure omitted). The sounding data at Tateno, which is located about

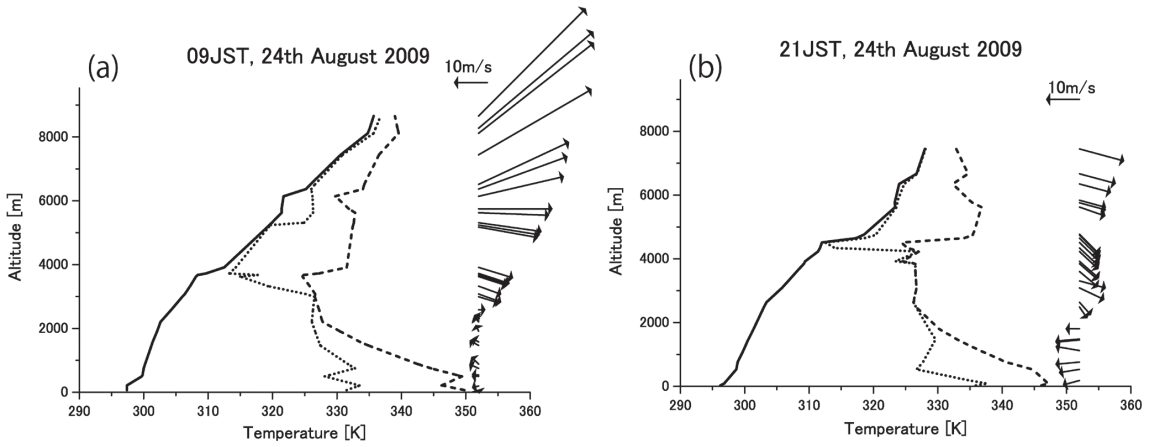

Fig. 3. Vertical profiles of potential temperature (solid lines), equivalent potential temperature (dotted lines), and saturated equivalent potential temperature (dashed lines) at (a) 0900 and (b) 2100 JST on August 24, 2009 at Tateno (140.125°E, 36.057°N). Vectors indicate the horizontal wind at each level.

90-km southeast from the Ka-band radar site, indicate that the atmosphere below the 4000-m level was convectively unstable at 0900 JST, while the air was dry and stable above the 4000-m level (Fig. 3a). At 0900 JST, CAPE, the lifted condensation level (LCL), and the level of free convection (LFC) were 66 J kg^{-1}, 895 m, and 2050 m, respectively, if an air parcel was lifted from 1000 hPa. At 2100 JST (Fig. 3b), the bottom of the stable layer was raised by about 1000 m although the profile did not experience significant change. CAPE, LCL, and LFC were 295 J kg^{-1}, 945 m, and 1850 m, respectively. Chuda and Niino (2005) statistically analyzed the sounding data from 1990 to 1999 for the whole of Japan and found that the median CAPE in August at Tateno was 1168 J kg^{-1}, which is larger than that in our study case. The wind profile at 0900 JST was characterized by weak easterly wind in the lower layer (less than 2000 m) and west-northwesterly wind in the middle layer (from 3000 m to 5000 m). The vertical wind shear from 1469 m to 5178 m is east-southeastern (110 degrees) and 5.5 m s^{-1} km^{-1}.

3.2 Surface precipitation, wind, and humidity

Figure 4 shows the distribution of 24-h rainfall on August 24, 2009 derived from Radar/Raingauge Analyzed Precipitation data of JMA. Several scattered areas of rainfall greater than 30 mm was recorded around the Ka-band (Kanuma) and X-band (Moka) radar sites. The convective rainfall studied here is located to the west and north of Moka and developed in the afternoon of the case study day.

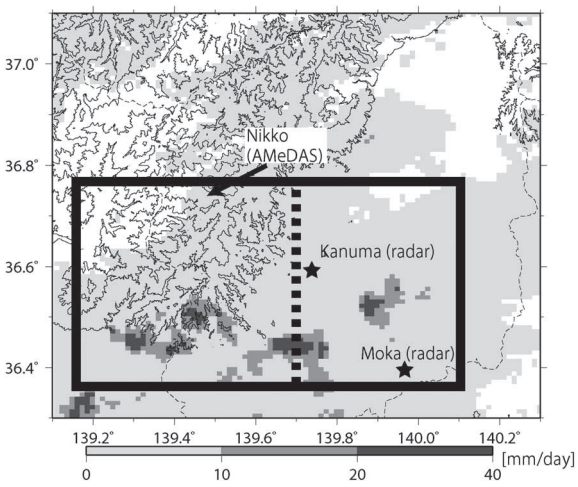

Fig. 4. Daily rainfall amount [mm] on August 24, 2009 derived from JMA Radar/Raingauge Analyzed Precipitation data. The areas with solid and dotted boundaries indicate the analysis area and the boundary of mountains used in Fig. 8, respectively. Topographic contours are drawn at 500-m intervals.

Figure 5 shows the distribution of surface wind observed by AMeDAS in northern Kanto area from 1200 to 1500 JST. Thin dashed lines indicate the boundary of the "sea breeze", defined as easterly or southerly wind greater than 1.5 m s^{-1} continuously spreading from the coast. At 1200 JST, the sea breeze did not reach the foot of the mountains, while

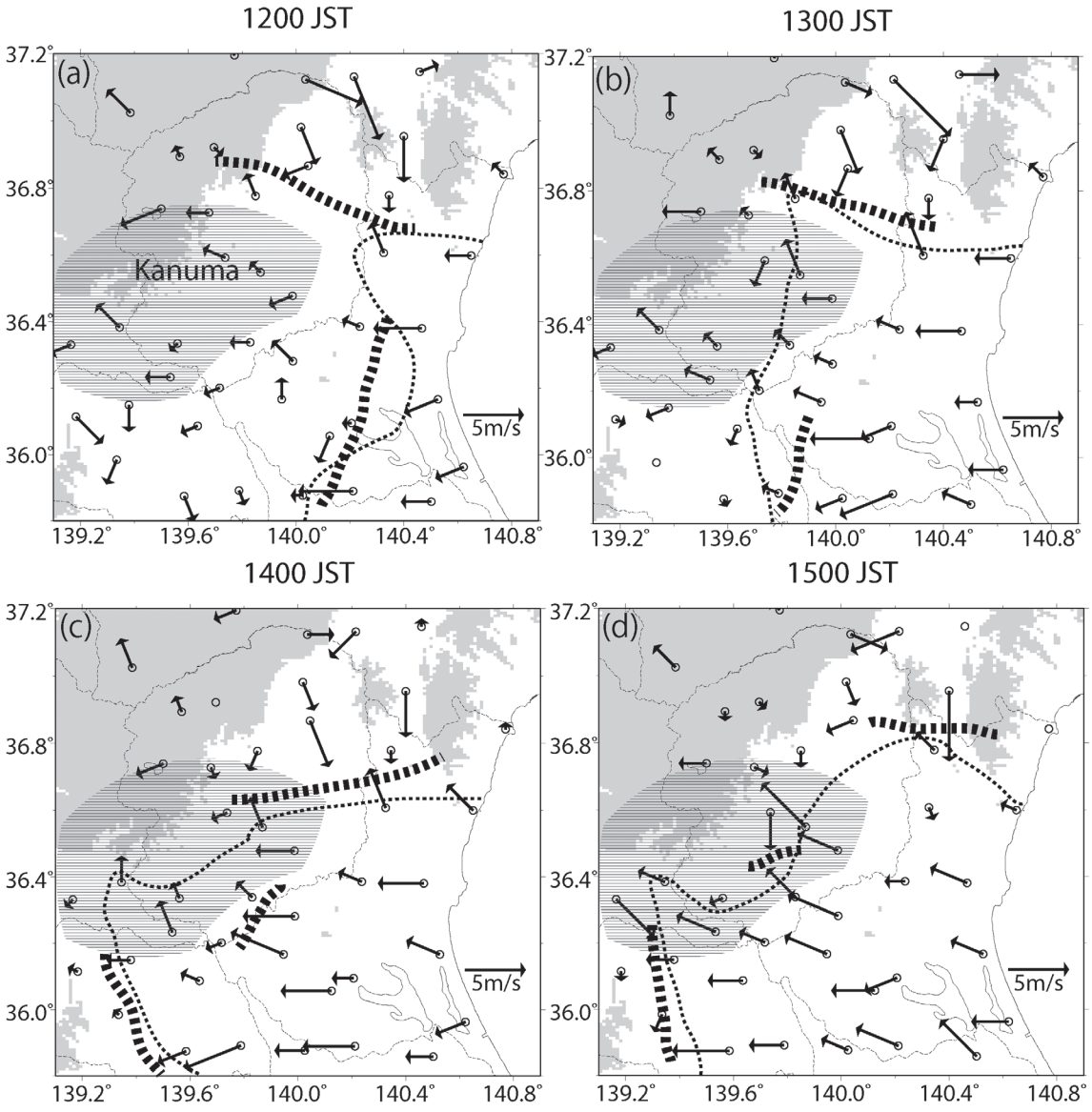

Fig. 5. Surface wind obtained by AMeDAS on August 24, 2009. Arrows indicate horizontal wind vectors at the surface. Thin dashed lines are boundaries of "sea breeze" defined as easterly or southerly wind greater than 1.5 m s^{-1} continuously spreading from the coast. Thick solid lines are convergence lines drawn subjectively. Areas higher than 500 m are shown by gray shading, and the range of dual Doppler analysis is shown by light shadings.

southeasterly wind from the foot of the mountains to the crest was observed around our observation area (light shaded area). This southeasterly is considered to be a part of valley wind circulation. From 1300 JST to 1400 JST, the sea breeze intruded further inland and reached the observation area (Figs. 5b, c). On the other hand, a northerly wind formed a convergence line with the southeasterly (thick dashed line), and parts of the convergence lines were found in the range of the X-band radars at 1400 JST and 1500 JST.

To see detailed development of the surface meteorological data, time series of surface wind at Kanuma (foot of the mountain) and the AMeDAS Nikko site (near the crest of the mountain) are shown in Fig. 6. At Kanuma, a southeasterly wind prevailed from 0900 to 1130 JST, and then easterly and

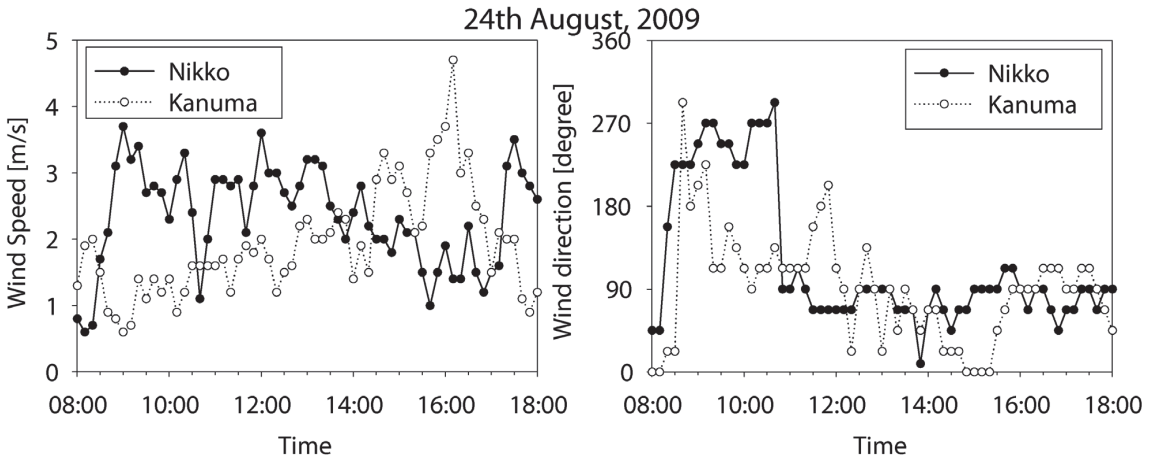

Fig. 6. Time variations of wind speed and direction at Nikko (near the crest of the mountain) and Kanuma (at the foot of the mountain) on August 24, 2009.

northeasterly wind prevailed. At Nikko, westerly wind prevailed until 1050 JST, and then the wind direction suddenly changed to the east. The wind speed is lower than 5 m s^{-1} in both places. Specific humidity at Kanuma gradually decreased until 1200 JST, and increased around 1330 JST and 1530 JST (Fig. 7) corresponding to the increase of wind speed (Fig. 6). GPS precipitable water observed a minimum value at 0900 JST and the maximum at 1500 JST, and then decreased. At Nikko, a rapid increase of specific humidity of about 2 g kg^{-1} was observed from 1040 to 1130 JST corresponding to the change of wind direction from the west to the east.

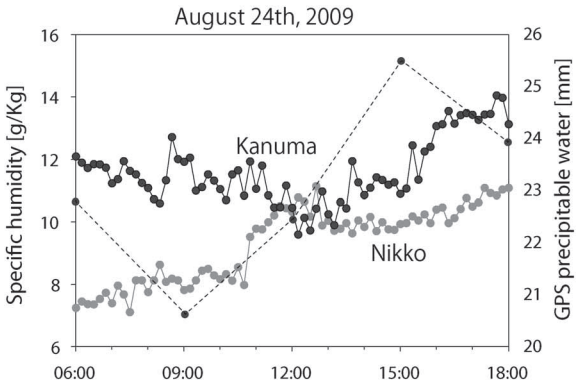

Fig. 7. Time series of specific humidity (black solid line) and GPS precipitable water (dotted line) at Kanuma, and specific humidity at Nikko (gray solid line).

3.3 Diurnal variation of radar echoes

During the analysis period, a diurnal change in the spatial distribution of convective clouds is clearly shown. We chose a rectangular area containing the mountain-plain boundary in a N-S direction along 139.7°E (Fig. 4) to investigate the spatial variation in X-band radar reflectivity. Figure 8 shows radar reflectivity at the 3.75-km level averaged along the latitudinal direction after the observation starting time (1006 JST). The dotted line in this figure indicates the boundary of the mountains defined by the altitude around 500 m, where the topography becomes steep. As a result, development of convective echoes is divided into three stages: 1) No echo was observed in the domain (stage 1; 1006 to 1200 JST), 2) echoes were limited over mountains (stage 2; 1200 to 1400 JST), and 3) echoes moved toward the plain and developed (stage 3: 1400 to 1600 JST). 1200 JST is the time when the X-band radar observed strong radar echoes for the first time.

For analysis of the X-band radar data, we defined "convective echo," "echo group," and "convective cell" to identify the echoes. Figure 9 is the schematic illustration of these definitions. A convective echo is defined as having radar reflectivity more than 8 dBZ with a closed contour at the 3.75-km level. If a new convective echo appeared in the north-to-northwest or the east-to-southeast direction within 10 km of a pre-existing convective echo, then both are assumed to belong to the same echo group. If a new convective echo appeared in a direction orthogonal to the movement of a pre-existing convective echo, the new

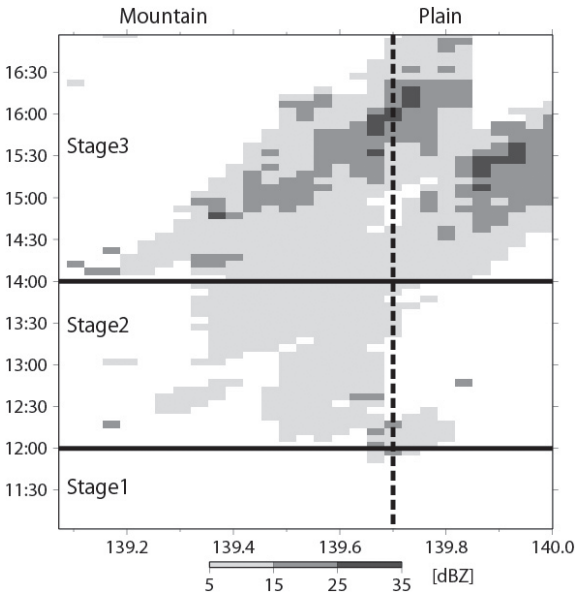

Fig. 8. Longitude-time section of radar reflectivity observed by the X-band radar at the 3.75-km level on August 24, 2009 averaged along the latitudinal direction of the rectangular region in Fig. 4. The broken line indicates the boundary between the mountains and the plain.

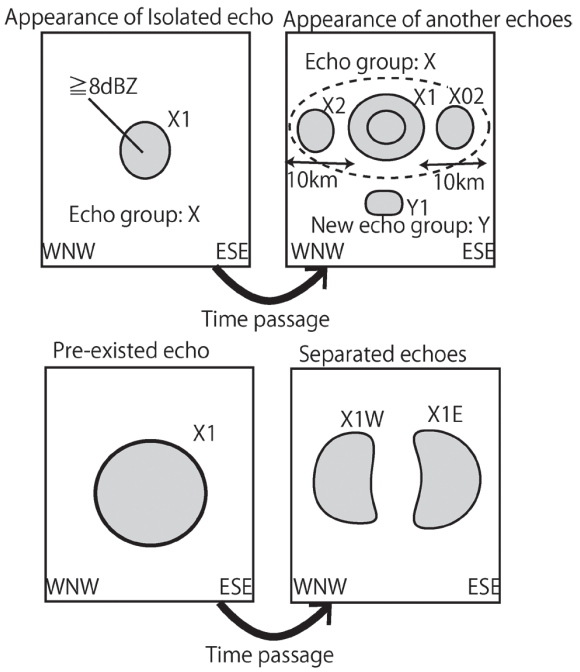

Fig. 9. Schematic illustrations of the horizontal distribution of a "convective echo," "echo group," (upper figure) and separated echoes (lower figure).

echo is assumed to form a new echo group. Furthermore, if a new convective echo appeared with a time lag, we looked up other heights of CAPPI and if we recognized that the new convective echo formed consecutively, we assumed them to belong to the same echo group. From these criteria, echo groups are named A, B, C, etc. in formation order, and convective echoes in the same echo group are called A1, A2, A3, etc. In particular, when a new convective echo appeared in the east-to-southeast direction of a pre-existing convective echo, we assigned it with "0" (e.g., X02). In cases of split convective echoes, each echo name was denoted by its direction; the western part of the convective echo with W and eastern part with E (e.g., A1W and A1E). In the case of the merger of several echoes, the merged convective echo takes the name of the echo with the strongest reflectivity before merging. In addition, convective cells were defined by reflectivity maxima over 17 dBZ in a convective echo. The term "convective clouds" is used for photographic images of clouds.

3.4 Characteristic of convective clouds in stage 1

During stage 1, there were no echoes observed by the X-band radars and a very small fraction of echoes was observed by the Ka-band radar. Therefore, we will explain the behavior of clouds only by the result of stereo photogrammetric analysis. The maximum cloud-top height in stage 1 reached 4000 m for a few minutes at around 1107 JST, and quickly declined (Fig.10a). Simultaneously, a small radar echo was observed by the Ka-band radar (figure omitted). During almost all of stage 1, the cloud top was suppressed to less than 4000 m. After 1146 JST, the cloud-top height were maintained higher than 4000 m and reached 6000 m at 1207 JST (Fig. 10a). Fig. 10b is the time series of moving speed and direction of convective clouds calculated by the stereo photogrammetric analysis. The velocities were calculated from the difference of the position at each time interval. The moving speed varies from 5 to 15 m s^{-1} and the direction was around 100 degrees (east-southeastward), which corresponds to the wind direction from the 3- to 5-km level at Tateno sounding at 0900 JST (Fig. 3). Figure 11 shows the horizontal distribution of the maximum cloud-top height at each time. These results show that the maximum cloud-top heights were between 1500 and 6000 m, and that the positions of clouds were limited in

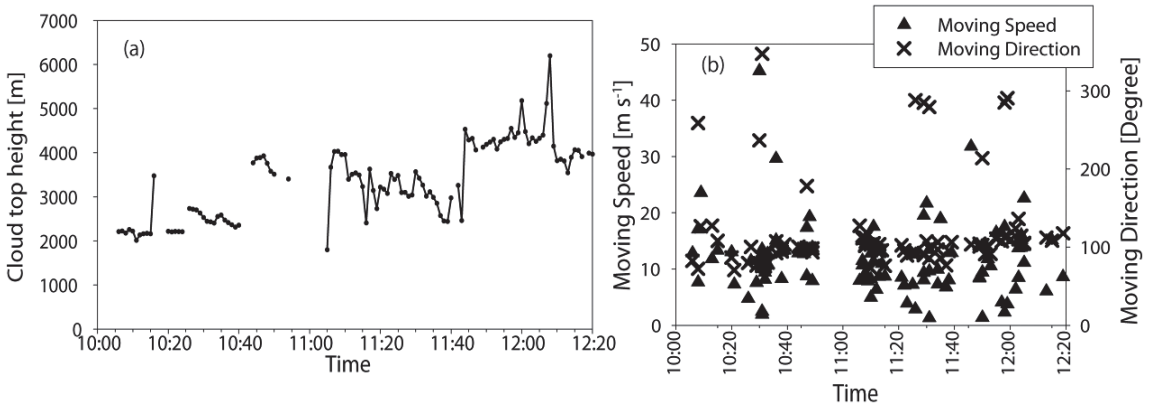

Fig. 10. (a) Time series of maximum cloud-top height of convective clouds calculated by stereo photogrammetric analysis. The cloud-top height in this figure is the maximum height in the whole photograph area (not of the individual cloud). (b) Time series of moving speed and direction of convective clouds calculated by stereo photogrammetric analysis.

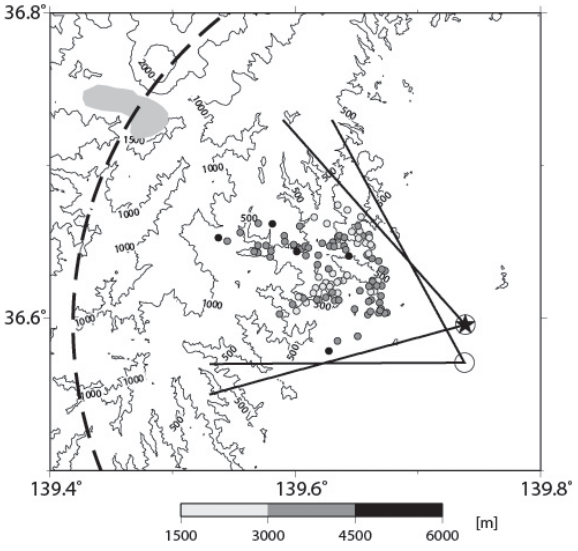

Fig. 11. Horizontal distribution of the maximum cloud-top heights and the position in each image calculated by stereo photogrammetric analysis from 1006 to 1221 JST. Circles and star symbols indicate the location of the cameras and the Ka-band radar, respectively. The gray shaded area indicates Lake Chuznji in Nikko.

the mountainous area. The distance between the points of clouds and the cameras was about 20 km. Therefore, if we assume the moving speed of clouds to be 10 m s^{-1}, the cloud must have reached the camera site in 30 min. However, no convective clouds reached the camera site in stage 1. In fact, the images of clouds became vague and dissipated before they reached the camera site.

3.5 Characteristic of convective echoes in stages 2 and 3

a. General characteristics

Figure 12 shows the tracks of convective echoes in stages 2 and 3. In this figure, convective echoes initiated and developed inside the dual Doppler analysis area are shown. Echoes were plotted at their geometric center at 5-min intervals. Tracks of convective echoes are slightly complicated because of their merger and split, but they still reflect the tendency of their movement. From this result, only echo groups A and H moved to the plain area in stage 2. During stage 2, all convective echoes developing over the mountains moved in the direction of the wind around the 3- to 5-km level at Tateno (Fig. 3); when they reached the foot of mountain, they quickly dissipated except echo groups A and H.

The convective echoes with names written with "(3)" in Fig. 12 formed in stage 3. During stage 3, there were some convective echoes such as F2, F3, and K1, which developed over the mountains, and did not dissipate even after reaching the foot of the mountains. In particular, convective echo K1 continuously moved toward the plain and its direction changed to the south after reaching the plain. Convective echo J1 formed in the plain area and also developed there.

Figure 13 shows the initiation points of new convective echoes relative to pre-existing ones. Black dots indicate the convective echoes in stage 2, and cross marks indicate those in stage 3. Thus, new convective echoes tend to form to the west or

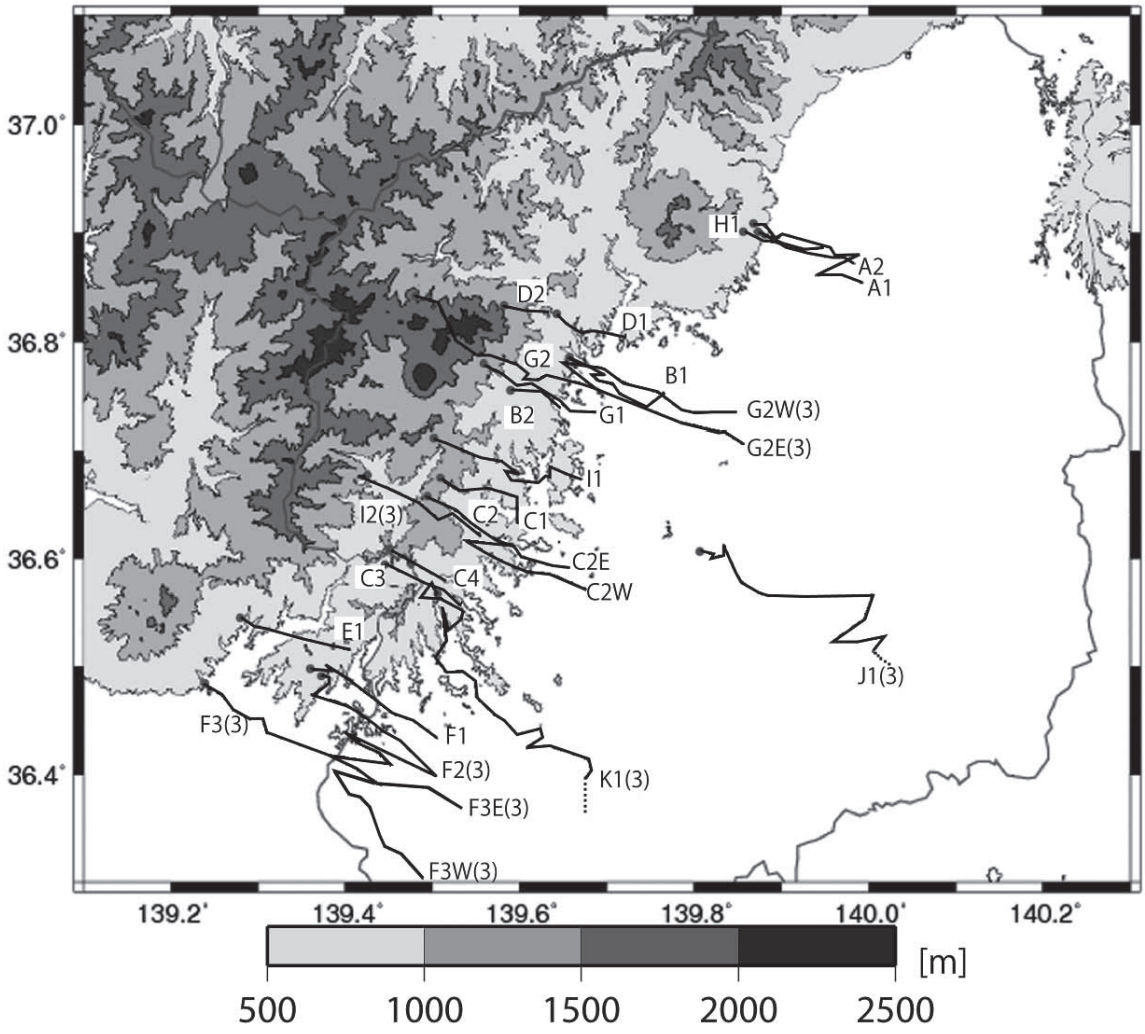

Fig. 12. Tracks of convective echoes in stages 2 and 3. Topographic contours are drawn every 500 m. Labels with "(3)" indicate the convective echoes in stage 3.

northwest of pre-existing echoes. Regarding the location of formation and dissipation, convective echoes in stage 2 developed over the mountains and dissipated over mountains or at the foot of the mountains.

Figure 14 shows the histograms of maximum echo-top heights, maximum reflectivity, and duration of convective echoes in stages 2 and 3. From this result, maximum echo-top heights were about 4000 to 6500 m in stage 2, while there is an echo reaching 8500 m in stage 3 (Figs. 14a, b). As a result, it is suggested that convective echoes were enhanced as the stage progressed. Stage 3 includes some weak echoes and also some very strong echoes (Fig. 14d). Many convective echoes were maintained for relatively short periods (less than 70 min) in stage 2, while there were two echoes that persisted for more than 120 min in stage 3 (Fig. 14f).

Figure 15 shows the longitude-height cross section of vertical velocity derived from dual Doppler radar analysis to elucidate the mean structure of vertical motion. The values are averaged in time and the latitudinal direction of the rectangle in Fig. 4. There are two downdraft areas in stage 2: one is around 139.4°E, corresponding to a high mountain, and the other is around 139.6°E near the mountain foot. Weak updraft exists between the downdrafts. In stage 3 (Fig. 15b), deep updraft covers from the mountains to the plain.

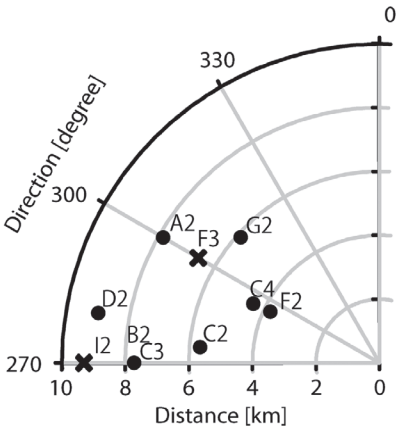

Fig. 13. Initiation points of new convective echoes relative to pre-existing echoes. Black dots and cross marks indicate the echoes in stages 2 and 3, respectively. (0,0) indicates the position of the pre-existing echo.

This suggests that the mesoscale circulation around the mountain slope became stronger and deeper in stage 3 than that in stage 2.

b. Structure of convective echoes C1 and C2 (stage 2)

Echo group C includes the convective echoes C1, C2, C3, and C4. Here we explain the structure of C1 and C2 as typical convective echoes in stage 2. This echo group initiated and ended over a mountainous area (Fig. 12).

At 1212 JST, convective echo C1 appeared with reflectivity of 20 dBZ (Fig. 16a). The topographic altitude of this point is about 1000 m. At 1222 JST, a new convective echo C2 formed to the west-northwest (mountain side) of C1 when C1 was weakening (Fig. 16b). At 1242 JST, west-northwestern wind prevailed in C2 and updraft/downdraft are located to the west (mountain)/east (foot of the mountain) (Figs. 16c, d). The reflectivity was about 20 dBZ. From the Ka-band radar at 1235 JST, C1 was almost dissipating and C2 was developing behind it (Fig. 17a), and at 1241 JST, C1 was dissipating and C2 was developing to the rear (Fig. 17b). C2 had two strong maxima of echoes with 25 dBZ, while only one maximum of echoes was detected by the X-band radar (Fig. 16d). Because the spatial resolution of the X-band radar is coarser than that of the Ka-band radar, the fine structure of convective echo C2 could not be resolved. After 1241 JST, convective echoes C2 kept the multi-cell structure, and moved to the foot of the mountains and

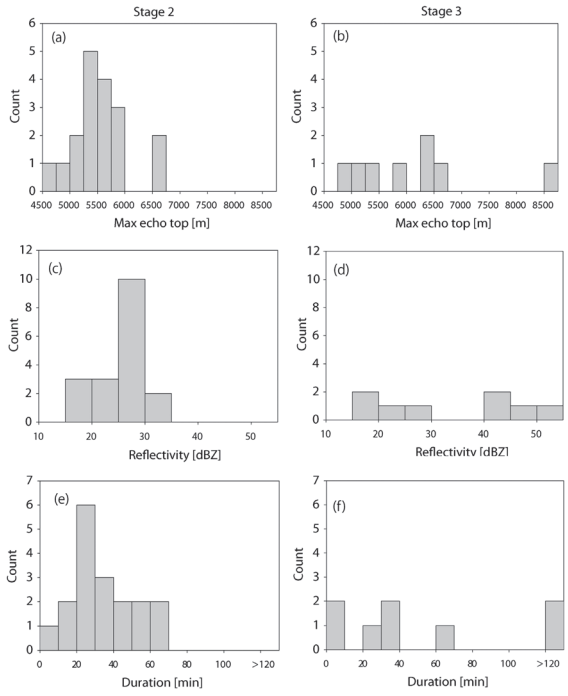

Fig. 14. Histograms of maximum echo-top heights (top), maximum reflectivity (middle) and duration (bottom) of convective echoes observed by X-band radar in stage 2 (left panels) and stage 3 (right panels).

dissipated (figure omitted).

c. Convective echo that formed in the plain area (J1)

Convective echo J1 formed in the plain area in stage 3 along the convergence line shown in Fig. 5, and became the second-strongest echo detected in this study. Such an echo was not observed before stage 3. At 1402 JST, convective echo J1 formed (Fig. 18a). After this time, J1 stagnated in this location. At 1427 JST, a new cell formed in the northern part of J1 (Fig. 18b). From 1442 to 1447 JST, another convective echo formed and merged with J1 (figure omitted), and at 1447 JST, the original J1 developed strongly (Fig. 18c). In addition, at 1447 JST, a new convective echo appeared on the southwestern side of J1 (Fig. 18c) and merged with echo J1 at 1457 JST (Fig. 18d). Due to the merging of several convective echoes, the area of J1 became large. After this time, J1 maintained its area and moved to the southeast. At 1457 JST, J1 has changed into a band running from the west-southwest to the east-northeast with a strong echo area (47 dBZ), where strong updrafts were observed (Fig. 18e). After 1452 JST, J1 moved out of the observation range of the

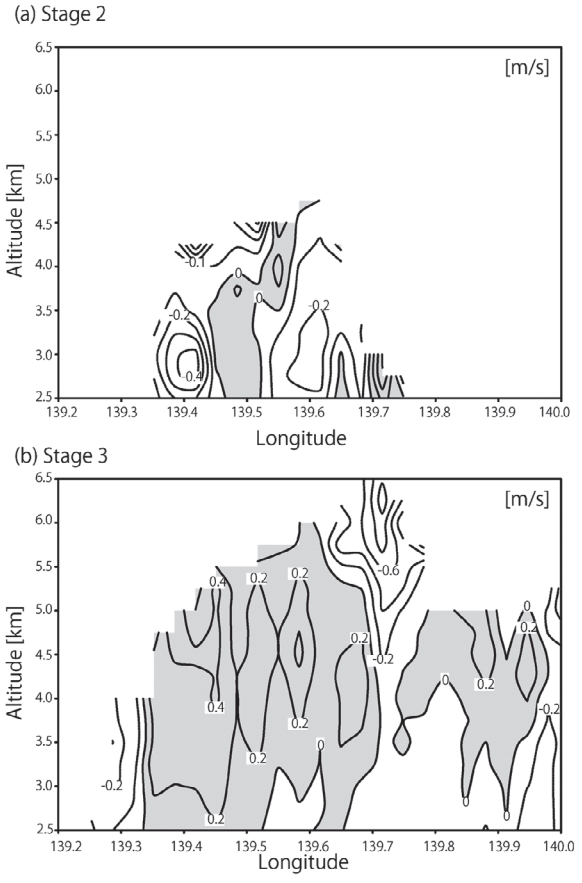

Fig. 15. Longitude-height cross sections of vertical velocity averaged along the latitudinal direction in the rectangle of Fig. 4 for the period of (a) stage 2 and (b) stage 3. Shaded areas indicate the updraft regions.

X-band radar. According to the JMA radar, J1 dissipated at 1650 JST.

Convective echo J1 had stronger vertical velocity than echo group C in stage 2. J1 had a duration longer than 120 min (according to the JMA radar, J1 persisted for about 180 min), which was considerably longer than those of echo group C. This was because J1 experienced replacement of cells and mergers with other small convective echoes.

d. Most developed convective echo (K1)

Convective echo K1 formed over the mountains in stage 2 and moved toward the plains in stage 3 without dissipating at the foot of the mountain, and was the most developed convective echo detected in this study. K1 formed at 1357 JST over the mountain slope at almost the same location as C4 (Fig. 12). From 1417 JST, K1 started to extend to the southeast and developed intensively (figure not shown). At 1457 JST, K1 had two convective cells (Fig. 19a), and the northwestern cell formed after the generation of southeastern cell (figure omitted). Therefore, the secondary cell formed on the upshear side of the pre-existing cell, which is similar to the echoes in stage 2. However, at 1507 JST, a new convective cell formed to the downshear (southeastern) side of pre-existing cells and started developing (Fig. 19b). After 1507 JST, convective cells repeatedly formed and merged together. Finally, at 1557 JST, K1 reached higher than 7000 m and had strong updraft on the upshear side and downdraft on the downshear side (Fig. 19d). After 1602 JST, K1 moved out of the Moka X-band radar observation range. According to the JMA radar, K1 continued to move to the south.

In summary, convective echo K1 was maintained due to the existence of several convective cells, similar to J1, and K1 reached the highest echo-top height and the strongest maximum reflectivity of 50 dBZ. Convective echo K1 formed a new convective cell to the northwestern side of the pre-existing convective cells, while after reaching the plain, K1 formed new convective cells to the downshear (southeastern) side, and these cells developed strongly.

4. Discussion

4.1 Relationship between convective activity and wind circulation

According to the spatial distribution of echoes observed by the X-band radar, convective activities were divided into three stages: 1) No echo was observed in the domain (stage 1: 1006 to 1200 JST), 2) Echoes were limited to over the mountains (stage 2: 1200 to 1400 JST), and 3) Echoes moved toward the plain and developed intensively (stage 3: 1400 to 1600 JST) (Fig. 8). Such variations of convective activity are considered to be related to the development of the local wind circulation. Here, we discuss the relationship between the behavior of convective clouds and the wind patterns.

During stage 1, the surface wind was southeasterly at the foot of the mountain (Kanuma) and westerly at the mountain (Nikko) until 1050 JST (Fig. 6). After 1050 JST, the wind direction near the mountain top (Nikko) changed from west to east, and specific humidity simultaneously increased by about 2 g kg^{-1} (Figs. 6 and 7). Kimura and Kuwagata (1995) pointed out that moisture is transported from the foot of the mountain to the crest by the valley wind circulation. The increase of the specific humidity at Nikko may be

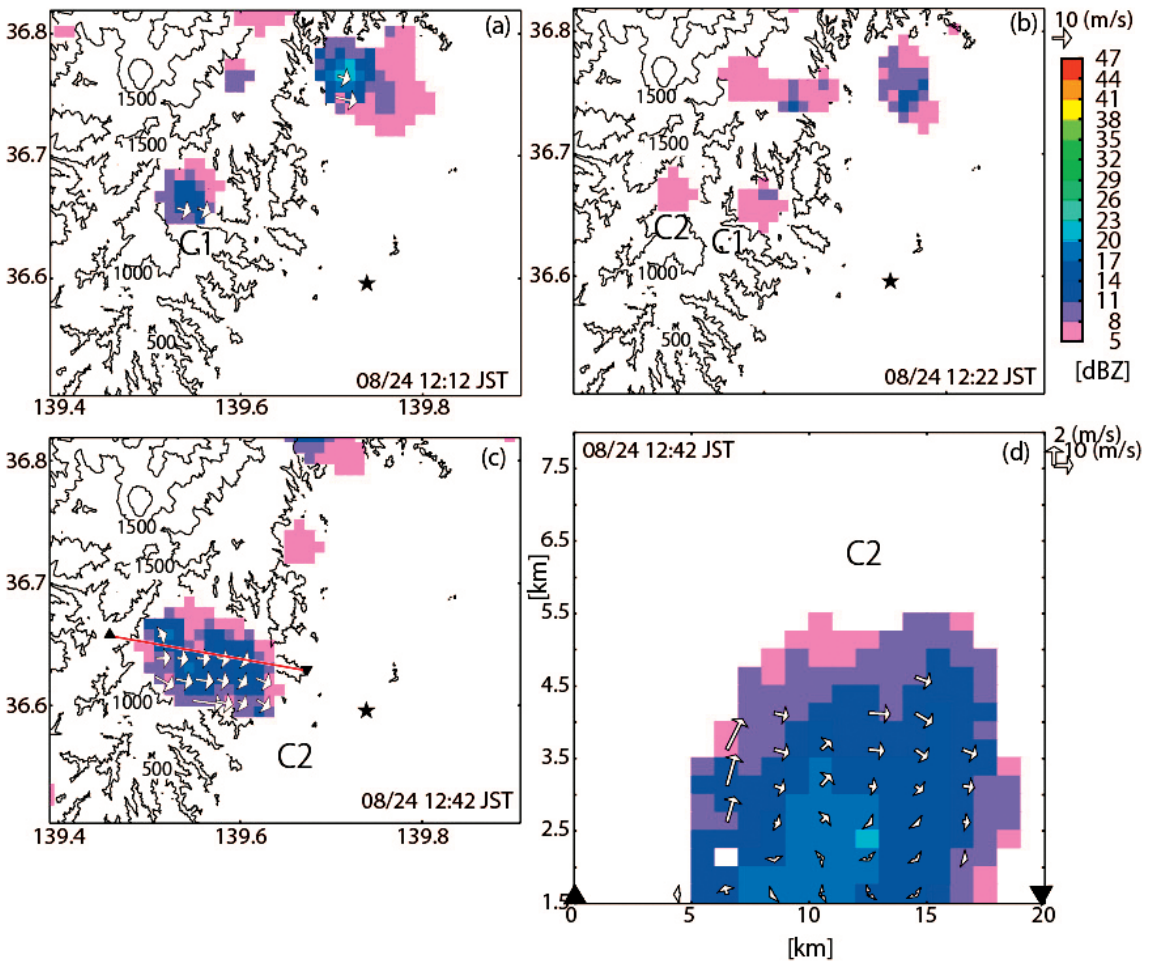

Fig. 16. Horizontal cross sections of radar reflectivity and wind vectors (ground relative) at the 3.75-km level at (a) 1212 JST, (b) 1222 JST, and (c) 1242 JST. Stars indicate the Ka-band radar site. Topographic contours are drawn every 500 m. (d) Vertical cross section of reflectivity and wind vectors along the red line in (c).

explained by the moisture transport by the valley wind. In stage 1, due to the stable layer around 4000 m, the convective clouds in this stage could not penetrate into the higher level. Kimura and Kuwagata (1995) also pointed out that the downdraft field is formed at the foot of the mountains as a compensation flow for the updraft on the mountain slope. Although such a downdraft field was not directly observed in stage 1, Doppler radar analysis in stage 2 indicated the existence of a downdraft around the foot of the mountains (Fig. 15a). The effect of the downdraft is one possible explanation for the dissipation of convective clouds at the foot of the mountains in stage 1. Behavior of convective clouds in stage 1 is schematically illustrated in Fig. 20a.

During stage 2, the surface wind at the foot of the mountain (Kanuma) was slightly enhanced compared to stage 1 (Fig. 6). The specific humidity at Kanuma started to increase after 1300 JST (Fig. 7). Initiation of convective echoes in the mountains and dissipation at the foot of the mountains were repeatedly observed by the X-band radar (Fig. 12). Thus, there was no change in the behavior of convective clouds from stage 1, except the appearance of radar echoes. In this stage, new convective echoes formed to the west-northwest of pre-existing ones (Fig. 13). Generally, in cases of the existence of cold outflow at a low level, strong horizontal convergence tends to form on the down-shear side (e.g., Weisman and Klemp 1982). In the present case, the echoes were weak (about 20 dBZ) and

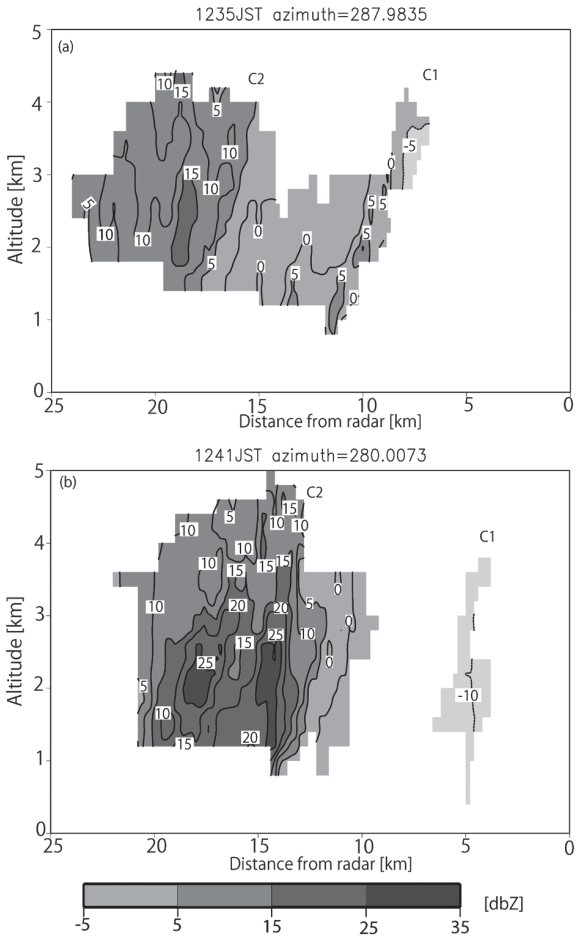

Fig. 17. Vertical cross sections of reflectivity of echo group C observed by the Ka-band radar [dBZ].

no outflow was observed by the dual-Doppler radar wind analysis. Therefore, new convective echoes might be triggered by the valley wind on the mountain slope, rather than the cold outflow. For example, convective echoes C1 and C2, C3 and C4, and F1 and F2 appeared at almost the same location, respectively (Fig. 12), indicating that there were favorable locations for their initiation. The wind circulation and behavior of convective echoes in this stage is schematized in Fig. 20b.

The Ka-band radar detected cellular echoes with a horizontal scale of about 1 km within a convective echo in stage 2 (Fig. 17). The existence of such small-scale cellular echoes was also pointed out by Sakurai et al. (2012) from their Ka-band radar observation. Unfortunately, the Ka-band radar could observe only a few convective systems in the present study, and thus it is difficult to discuss the formation and maintenance process of such structures. We need to accumulate more observational data with Ka-band radar to elucidate the fine structure of convective clouds.

During stage 3, initiation and movement of some convective echoes were different from those in stages 1 and 2. Moreover, some convective echoes developed to higher level and stronger reflectivity than that in stage 2 (Fig. 14). Therefore, some other processes were operating in this stage. Precipitable water at the foot of the mountain (Kanuma) showed the minimum at 0900 JST and the maximum at 1500 JST, and then it gradually decreased (Fig. 7). This phenomenon was similar to that found by Sato and Kimura (2003, 2005) except that the maximum occurred two hours earlier. Sato and Kimura (2003, 2005) indicated that the high precipitable water formed over the mountains is advected toward the foot of the mountains by the environmental wind in the late afternoon. They also showed that low convective instability index (CII) formed over plain area and led to a favorable condition for convective cloud development. Because the variation of precipitable water and the direction of the environmental wind in this study were consistent with theirs, the development of echoes over the plain in stage 3 could be explained by the increase of instability due to the advection of water vapor before this stage. In the present study, the movement of convective clouds from mountains to the plain in stages 1 and 2 suggest the transportation of moisture to the plain before the convective initiation in stage 3.

There was a convergence zone between the easterly and northerly wind in the observation area (Fig. 5). The convective echo J1 formed over this convergence zone. This fact implies that the mesoscale convergence also played an important role for the development of echoes in stage 3. However, we consider that the atmospheric instability is more important for the vigorous development of echoes, because the convergence line had already formed in the plain before this time (1400 JST) but no convective echo was produced before stage 3. The behavior of convective echoes in stage 3 is illustrated in Fig. 20c.

4.2 Comparison with previous observational studies

In the present study, some convective echoes formed over the mountains moved to the plain in stage 3. However, such behavior of convective echoes has not always been observed in previous studies. In this section, we compare our results with those of previous studies to discuss the difference in the behavior of convective systems. Bennett et al. (2011) conducted

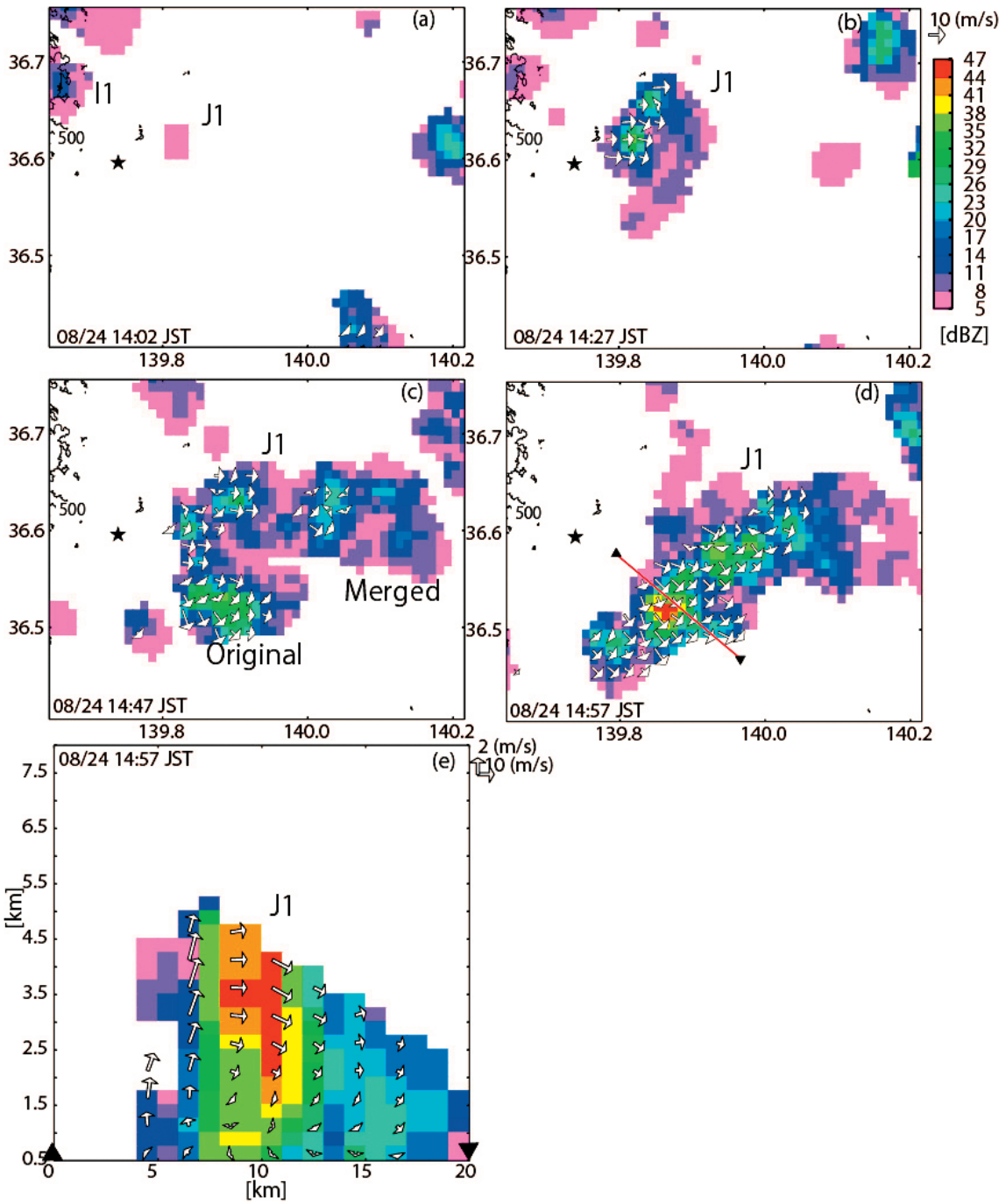

Fig. 18. Horizontal cross sections of radar reflectivity and wind vectors (ground relative) at the 3.75-km level at (a) 1402 JST, (b) 1427 JST, (c) 1447 JST, and (d) 1457 JST. Stars indicate the Ka-band radar site. (e) Vertical cross section of reflectivity and wind vectors along the red line in (d).

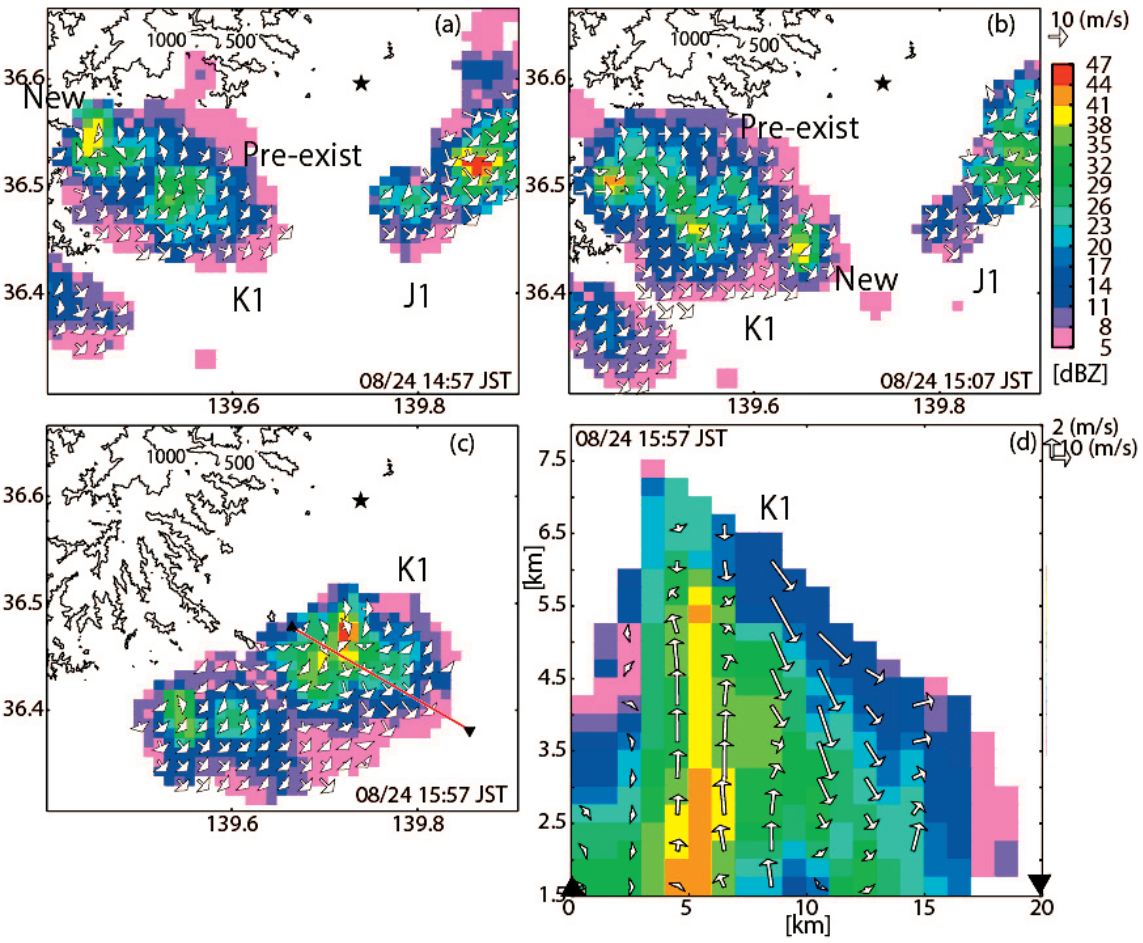

Fig. 19. Same as in Fig. 16 but for (a) 1457 JST, (b) 1507 JST, and (c) 1557 JST. (d) Vertical cross section along the red line in (c).

intensive observations and numerical simulation around a mountainous area in Germany and France. In cases of no significant synoptic-scale disturbance with weak CAPE (< 200 J kg^{-1}), they pointed out that the formation of the warm and moist core due to elevated surface heating and the convergence line produced by thermal flows affected the initiation of convection. In their case, the steering wind of convective clouds was from the plain to the mountain, which is opposite to that of our case. The convection was limited over mountains and there was no stage in which clouds moved over the plains. Sano and Tsuboki (2006) conducted an X-band dual-Doppler observation over the Nobi Plain and Ibuki Mountains, Japan. This area is composed of mountains, a plain, and an ocean, which are topographical features similar to those in our study area. However, convective echoes remarkably developed on the mountain slope, and they did not move over the plain area. Sano and Tsuboki (2006) pointed out that due to weak environmental wind and vertical shear, convective echoes stagnated on the mountain slope. In their case, the environmental wind was weaker than that in our study (wind speed at the 5-km level was 9 m s^{-1} in Sano and Tsuboki (2006), and 18 m s^{-1} in our study). Thus, we consider that the existence of strong midlevel wind from the mountain to the plain is necessary for the movement of convective clouds from mountains to plains.

5. Conclusions

The behavior and structure of convective clouds and echoes on August 24, 2009 around the northern Kanto mountain area were investigated using stereo photogrammetric analysis and Ka-band and X-band radars.

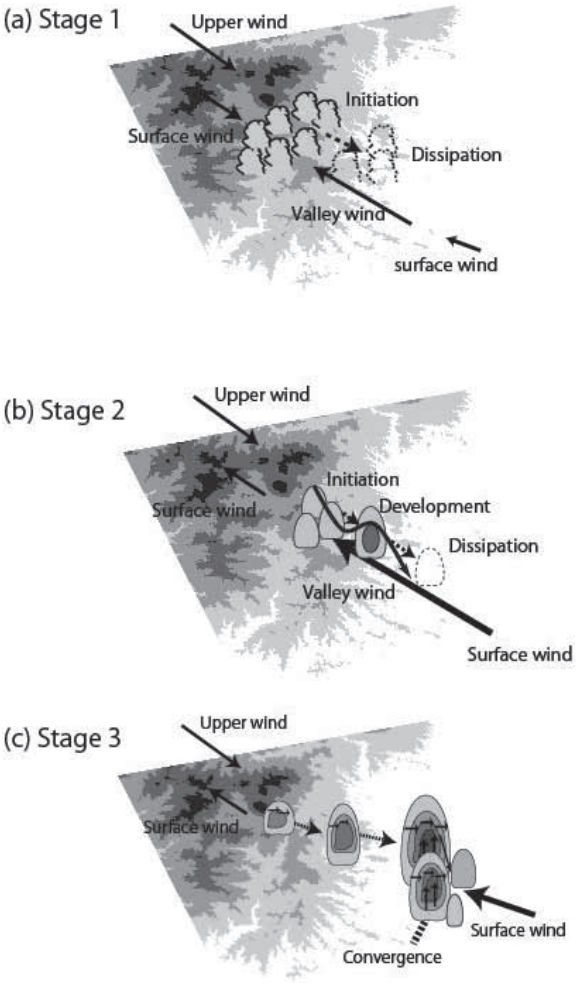

Fig. 20. Schematic illustrations of wind circulation and development of convective clouds (echoes) in (a) stage 1, (b) stage 2, and (c) stage 3.

The results are summarized as follows:

1) Convective activity around the mountain was divided into three stages: no echo (stage 1), echoes limited to the mountain area (stage 2), and echoes developing over the plain (stage 3).
2) During stages 1 and 2, the convective clouds or echoes initiated over the mountain, and then moved toward the foot of mountains and dissipated, repeatedly. During stage 3, convective echoes did not dissipate at the foot of the mountain and moved toward the plain while developing.
3) In stage 2, new echoes formed to the northwest (upshear) side of pre-existing echoes, while in stage 3, new cells sometimes formed to the southeast (downshear) side of pre-existing cells.
4) These stages of convective activities are considered to be related to the water vapor transportation by the valley wind and cloud advection by the midlevel wind. Further intensive observational study is necessary to elucidate this process.

The results in this study are considered to represent typical convective cloud development around the mountains. Our study reveals the detailed behavior and structure of convective clouds and echoes around the mountainous area, which had not been elucidated by conventional radars. Numerical simulation of this event and comparison to our results would be useful in checking the performance of a cloud-resolving model in simulating the behavior of convective clouds in each stage. Moreover, it is important to perform further observational studies of strong convective events to elucidate the effects of environmental conditions on the initiation and development processes.

Acknowledgments

The authors would like to thank Prof. T. Tanaka, Prof. N. Tase, Prof. M. Sugita, Prof. J. Asanuma, Prof. M. Tsujimura, and Dr. T. Yamanaka of University of Tsukuba hydrological science for their meaningful suggestions at presentations, the staff of Care House Namegawa and Kanuma Civic Culture Center for providing observation sites, and Dr. Seiichi Shimada of NIED for providing the GPS atmosphere delay data. The authors also thank Dr. Masayuki Kawashima of Hokkaido University and two anonymous reviewers for their helpful comments.

References

Barthlott, C., J. W. Schipper, N. Kalthof, B. Adler, C. Kottmeier, A. Blyth, and S. Mobbs, 2010: Model representation of boundary-layer convergence triggering deep convection over complex terrain: A case study from COPS. *Atmos. Res.*, **95**, 172–185.

Bennett, L. J., A. M. Blyth, R. R. Burton, A. M. Gadian, T. M. Weckwerth, A. Behrendt, D. P. Girolamo, M. Dorninger, S.-J Lock, V. H. Smith, and S. D. Mobbs, 2011: Initiation of convection over the Black Forest mountains during COPS IOP15a. *Quart. J. Roy. Meteor. Soc.*, **137**, 176–189.

Chuda, T., and H. Niino, 2005: Climatology of environmental parameters for mesoscale convections in Japan. *J. Meteor. Soc. Japan*, **83**, 391–408.

Cressman, P. G., 1959: An operational objective analysis system. *Mon. Wea. Rev.*, **87**, 367–374.

Fujibe, F., H. Seko, and Y. Shoji, 2003: Relation between precipitation distribution and surface wind patterns in the Kanto Plain in the afternoon of summer. *Tenki*, **50**, 777–786 (in Japanese).

Fukao, S., and K. Hamazu, 2009: *Radar remote sensing of weather and atmosphere*. Kyoto University Press, 502 pp (in Japanese).

Gao, J., and M. Xue, 1999: A variational method for the analysis of three-dimensional wind fields from two Doppler radars. *Mon. Wea. Rev.*, **127**, 2128–2142.

Horie H., and K. Tomine, 1998: A study on generation and movement of air mass thunderstorms over Kanto area in summer 1995. *Tenki*, **45**, 441–453 (in Japanese).

Iwasaki, H., 2004: Diurnal variations of precipitable water and convective activity with dual maxima in summer season around Mt. Tanigawa in the northern Kanto district, Japan. *J. Meteor. Soc. Japan*, **82**, 805–816.

Kalthoff, N., B. Adler, Ch. Barthlott, U. Corsmeier, S. Mobbs, S. Crewell, K. Träumner, C. Kottmeier, A. Wieser, V. Smith, and P. D. Girolamo, 2009: The impact of convergence zones on the initiation of deep convection: A case study from COPS. *Atmos. Res.*, **93**, 680–694.

Kimura, F., and T. Kuwagata, 1995: Horizontal heat fluxes over complex terrain computed using a simple mixed-layer model and a numerical model. *J. Appl. Meteor.*, **34**, 549–558.

Kojima, E., and H. Iwasaki, 2001: Some features on the merge of cumulonimbus clouds in summer season over the Kanto district. *Tenki*, **48**, 141−149 (in Japanese).

Kondo, H. 1990a: A numerical experiment of the extended sea breeze over the Kanto Plain. *J. Meteor. Soc. Japan*, **68**, 419–434.

Kondo, H., 1990b: A numerical experiment on the interaction between sea breeze and valley wind to generate the so-called extended sea breeze. *J. Meteor. Soc. Japan*, **68**, 435–446.

Naito, I. (ed.), 1998: *GPS meteorology*. *Meteorological Research Note*, **192**, 220 pp (in Japanese).

Nakamura, M., T. Kato, and S. Hayashi, 2011: Reproducibility of diurnal variation of summertime precipitation by a nonhydrostatic model. *WGNE blue book*, *Res. Activ. Atmos. Oceanic Modell.*, Section 2, 9–10.

Park, S. G, V. N. Bringi, V. Chandrasekar, M. Maki, and K. Iwanami, 2005: Correction of radar reflectivity and differential reflectivity for rain attenuation at X band. Part 2: Evaluation and application. *J. Atmos. Oceanic. Technol.*, **22**, 1633−1655.

Saito, T., and F. Kimura, 1998: Diurnal variation of convective precipitation in Chubu-Kanto area in the summer. *Tenki*, **45**, 541−549 (in Japanese).

Sakurai, N., K. Iwanami, T. Maesaka, S. Suzuki, S. Shimizu, R. Misumi, D. Kim, and M. Maki, 2012: Case study of misoscale convective echo behavior associated with cumulonimbus development observed by Ka-band Doppler radar in Kanto region. *SOLA*, **8**, 107−110.

Sano, T., and K. Tsuboki, 2006: Structure and evolution of a cumulonimbus cloud developed over a mountain slope with the arrival of sea breeze in summer. *J. Meteor. Soc. Japan*, **84**, 613–640.

Sato, T., and F. Kimura, 2003: A two-dimensional numerical study on diurnal cycle of mountain lee precipitation. *J. Atmos. Sci.*, **60**, 1992–2003.

Sato, T., and F. Kimura, 2005: Diurnal cycle of convective instability around the central mountains in Japan during the warm season. *J. Atmos. Sci.*, **62**, 1626−1636.

Sawada, Y., and H. Takahashi, 2002: Occurrence and Migration of Meso-β-scale precipitation area over the Kanto District in summer. *Geographical Review of Japan*, **75**, 509–528 (in Japanese).

Shimizu, S., and T. Maesaka, 2007: Multiple Doppler radar analysis using variational technique to retrieve three-dimensional wind filed. *Report of the National Research Institute for Earth Science and Disaster Prevention*, **70**, 1–8 (in Japanese with English abstract).

Weisman, L. M., and J. B. Klemp, 1982: The dependence of numerically simulated convective storms on vertical wind shear and buoyancy. *Mon. Wea. Rev.*, **110**, 504–520.

Zhender, A. J., J. Hu, and R. Anshuman, 2007: A stereo photogrammetric technique applied to orographic convection. *Mon. Wea. Rev.*, **135**, 2265–2277.

Zhender, A. J., J. Hu, and R. Anshuman, 2009: Evolution of the vertical profile during the transition from shallow to deep convection during CuPIDO 2006. *Mon. Wea. Rev.*, **137**, 937–953.